CrossMark

RESEARCH PAPER

Sediment–well interaction during depressurization

Hosung Shin[1] · J. Carlos Santamarina[2]

Abstract Depressurization gives rise to complex sediment–well interactions that may cause the failure of wells. The situation is aggravated when high depressurization is imposed on sediments subjected to an initially low effective stress, such as in gas production from hydrate accumulations in marine sediments. Sediment–well interaction is examined using a nonlinear finite element simulator. The hydro-mechanically coupled model represents the sediment as a Cam-Clay material, uses a continuous function to capture compressibility from low to high effective stress, and recognizes the dependency of hydraulic conductivity on void ratio. Results highlight the critical effect of hydro-mechanical coupling as compared to constant permeability models: A compact sediment shell develops against the screen, the depressurization zone is significantly smaller than the volume anticipated assuming constant permeability, settlement decreases, and the axial load on the well decreases; in the case of hydrates, gas production will be a small fraction of the mass estimated using a constant permeability model. High compressive axial forces develop in the casing within the production horizon, and the peak force can exceed the yield capacity of the casing and cause its collapse. Also tensile axial forces may develop in the casing above the production horizon as the sediment compacts in the depressurized zone and pulls down from the well. Well engineering should consider: slip joints to accommodate extensional displacement above the production zone, soft telescopic/sliding screen design to minimize the buildup of compressive axial force within the production horizon, and enlarged gravel pack to extend the size of the depressurized zone.

Keywords Gas production · Hydrates · Hydro-mechanical coupling · Numerical simulation · Sediment–well interaction

1 Introduction

Sediment–well interaction is a classical soil–structure interaction problem in geomechanics, similar to pile foundation analysis but with a few important caveats and differences [23]. First, even if no axial load is imposed at the top of the well, the casing can be intensely loaded by the shear resistance mobilized as the sediment contracts at depth during the depressurization (analogous to negative skin friction). Second, the increase in effective stress against the production screen/pack alters the sediment properties. In contrast, piles are loaded at the top and the sediment response is determined by the initial conditions before the installation of the pile.

Depressurization-driven gas production from hydrate-bearing sediments is a case in point. Hydrate formation requires the presence of gas and water, and a combination of high water pressure and low temperature conditions that falls within the stability field [31]. Therefore, hydrate accumulations in marine sediments are found where the water column exceeds $\sim$400 m depth and in shallow

✉ Hosung Shin
shingeo@ulsan.ac.kr

J. Carlos Santamarina
Carlos.Santamarina@KAUST.EDU.SA

[1] Civil and Environmental Engineering, University of Ulsan, Ulsan 680-749, Korea

[2] Earth Science and Engineering, King Abdullah University of Science and Technology (KAUST), Thuwal 23955-6900, Saudi Arabia

Springer

sediments before the geothermal gradient brings the sediment temperature outside stability conditions. Consequently, hydrate-bearing marine sediments experience high fluid pressure u_o but low in situ effective stress σ'_o.

Gas can be recovered from hydrate-bearing sediments by depressurization, heating, chemical-driven dissociation (by shifting the phase boundary), and molecular exchange (e.g., CO_2–CH_4). Production strategies have been investigated using coupled THCM numerical simulators [1, 8, 10–13, 18–20, 22, 27, 32, 33]. These studies have emphasized the evolution of temperature and fluid pressure within the production horizon and their consequences on gas production. Depressurization appears to be the most viable alternative in sandy formations [16].

In general, the increase in effective stress $\Delta\sigma'$ in applications that involve depressurization can be many times higher than the initial effective stress in situ σ'_o, that is $\Delta\sigma' \gg \sigma'_o$ (Note: such is the case for depressurization-driven gas production from hydrate-bearing marine sediments). Then, the following changes are anticipated: large volume compaction around the screen/pack, marked increase in stiffness, and pronounced decrease in hydraulic conductivity. These changes are coupled and vary throughout the affected volume.

Sediment compaction in and around the depressurized horizon challenges the engineering design of wells [17]. Careful analysis is required to anticipate the consequences of depressurization, to properly engineer the well installation/termination, and to develop optimal production strategies. The study documented herein focuses on variables and processes that govern sediment–well interaction, explores unanticipated emergent phenomena, and suggests alternative engineering designs for bottom hole completion. Analyses address the prevalent role of hydro-mechanical coupling on sediment–well interaction. The case of gas production from hydrate-bearing sediments involves chemo-thermal effects during hydrate dissociation and related changes in hydraulic conductivity and stiffness; simulation conditions implemented herein explore asymptotic conditions after dissociation as fluid flow reaches steady state.

2 Finite element model

A fully coupled hydro-mechanical analysis is conducted to explore the consequences of depressurization. The complete length of the well is modeled to properly study the interaction between the sediment and the well. Special considerations related to the constitutive models used to represent salient processes are described first. These models are implemented in the multi-dimensional FEM simulator Geo-COUS (Geo-COUpled Simulator) specifically developed to investigate coupled phenomena in granular and/or porous media subjected to multi-phase flow.

2.1 Sediment constitutive model

2.1.1 Compressibility

The axi-symmetric finite element model consists of 8-node displacement and 4-node fluid pressure continuum elements. Given the large number of unknowns involved in this kind of problems, the sediment is represented as a robust Modified Cam-Clay (MCC) material using a consistent tangent modulus formulation [21, 28, 30]. MCC overestimates the peak deviatoric stresses on the dry side (we imposed the Hvorslev surface and tension cutoff—[28], and the associated flow rule is unable to predict peak deviatoric stress before the critical state commonly observed in normally consolidated undisturbed clays, and MCC fails to predict the observed softening and dilatancy of dense sands [9, 34]. However, prevalent stress paths throughout the production horizon in depressurization problems tend away from failure; therefore, the sediment compressibility $e = f(\sigma')$ is more important than its shear response away from the well–sediment interface, and model choices such as non-associativity and the shape of the plastic potential surface have diminishing effects.

The classical Terzaghi-type compressibility model $e = f(\sigma')$ in MCC is modified to avoid unrealistically high void ratios at low σ'_o near the seafloor and negative void ratios near the well where $\sigma'_o + \sigma'$ is high during depressurization(Chong and Santamarina [4] present a comprehensive list of possible functions),

$$e = e_{1kPa} - C_c \log\left(\frac{1\,\text{kPa}}{\sigma' + \sigma'_L} + \frac{1\,\text{kPa}}{\sigma'_H}\right)^{-1} \quad (1a)$$

Constants e_{1kPa} and C_c define the central part of the compressibility trend. Asymptotic low and high void ratios e_L and e_H determine the low and high stress constants σ_L and σ_H for a given sediment; from Eq. 1a

$$\sigma'_H = 10^{\frac{e_{1kPa} - e_H}{C_c}} \cdot \text{kPa} \quad \text{when } \sigma' \to \infty \quad (1b)$$

$$\sigma'_L = \frac{\sigma'_H}{10^{\frac{e_L - e_H}{C_c}} - 1} \quad \sigma' \to 0 \quad (1c)$$

Therefore, there are four model parameters: e_L, e_H, e_{1kPa}, and C_c. This single continuous function permits modeling the sediment without numerical discontinuities, everywhere in the formation and throughout its evolution following depressurization.

2.1.2 Hydraulic conductivity

The hydraulic conductivity k [cm/s] evolves with changes in void ratio, and it may have a pronounced effect on the hydro-mechanical coupled response. The following power equation properly captures the evolution of hydraulic conductivity with void ratio e [2, 3, 6, 7, 15, 26]:

$$\frac{k}{k_{\mathrm{ref}}} = \left(\frac{e}{e_{\mathrm{ref}}}\right)^b \quad (2)$$

where k_{ref} [cm/s] is the hydraulic conductivity at a preselected reference void ratio e_{ref}, and the b-exponent captures the sensitivity of hydraulic conductivity to changes in void ratio. The parameter k_{ref} is determined by the sediment specific surface and varies across 8+ orders of magnitude. The exponent ranges from $b \approx 2.5$ for sands to $b \approx 4$ and larger for clayey sediments (see [25] for model parameters k_{ref} and b based on an extensive database).

There are additional changes in hydraulic conductivity during gas production from hydrate-bearing sediments as the solid hydrate mass vanishes and the gas phase appears. These changes are not modeled in the hydro-mechanical simulations reported herein which place emphasis on end-conditions during steady-state seepage after dissociation.

2.2 Sediment–casing interface

2.2.1 Interface element

Thin hydro-mechanical interfacial elements are used to model the sediment–casing interface (6-node displacement and 4-node fluid pressure axi-symmetric elements, modified from Segura and Carol [29]). They have infinite transverse hydraulic conductivity, zero longitudinal conductivity, and quasi-infinite normal stiffness. The mobilized shear resistance τ is assumed elasto-plastic in terms of the relative shear displacement δ

$$\tau = k_s \delta \quad \text{for } \delta \leq \delta_y \quad (3a)$$

$$\tau_{\mathrm{ult}} = \sigma_r' \tan \phi \quad \text{for } \delta > \delta_y \quad (3b)$$

where δ_y is the yield displacement for sediment-wall shear; the ultimate shear strength τ_{ult} of the interface is proportional to the normal effective stress in the radial direction σ_r' and the sediment-casing friction angle ϕ (Coulomb model). The interface shear stiffness k_s increases as the normal effective stress increases. We capture this response by making k_s proportional to τ_{ult} through the yield displacement δ_y,

$$k_s = \frac{\tau_{\mathrm{ult}}}{\delta_y} \quad (4)$$

Then, the bilinear elasto-plastic shear response is completely defined by δ_y and ϕ.

2.2.2 Casing element

The casing is modeled using elastic axi-symmetric conical shell elements with 3-node displacement and rotation for displacement compatibility ([24]; casing stiffness $E = 200\,\mathrm{GPa}$, Poisson's ratio $\upsilon = 0.30$). The bottom of the casing is closed; in addition, there is an internal isolation plate that separates the production zone from the upper part of the casing. Above the isolation plate, the casing is subjected to internal hydrostatic pressure $u_o(z)$. Bellow the isolation plate, the internal fluid pressure evolves with the fluid pressure history that is imposed on the sediment. The internal fluid pressure acts against all "steel faces", i.e., the pipe, upper and lower faces of the isolation plate, and the bottom plate.

2.3 Numerical conditions for simulations

The case modeled here corresponds to depressurization within a marine sediment. However, the methodology and observed effects are general and apply to other hydro-mechanically coupled problems that involve depressurization.

2.3.1 Boundary conditions

The axi-symmetric well geometry has the following boundary conditions:

- Top sea-floor surface: zero vertical effective stress and constant fluid pressure
- Base and far-field radial boundary: zero normal strain, zero frictional resistance, and constant fluid pressure.

Preliminary studies showed marked effects of the lower and radial far-field boundaries. Then, boundaries were moved gradually away until all boundary biases vanished.

2.3.2 Initial conditions

The sediment is subjected to self-weight k_0: consolidation (gravitational field—normally consolidated condition—imposed Jacky's $k_0 = 1 - \sin\phi$). At the end of consolidation, the sediment unit weight satisfies Eq. 1 at all depths.

We assume that the well completion does not change the in situ state of stress, and there is no residual shear between the casing and the formation after installation. The initial state of stress against the well is a consequence of complex, case-specific drilling operations: drilling, mud weight, cake

formation, cement hydration, and volume change. Eventually, depressurization gains controls over the evolving effective stress; in fact, the change in effective stress can be greater than the initial vertical effective stress $\Delta\sigma' > \sigma'_o$ in producing wells from soft sediments.

The selected interface friction is the same as the internal frictional resistance of the surrounding sediment. We do not impose any reduction for "relative roughness" because wells are typically cemented in, and there is evidence that the mud cake becomes cemented as well. Therefore, interfacial failure will take place within the sediment if a proper cement job is executed and outside the gravel pack in the production horizon. On the other hand, the parametric study—discussed later—covers a wide range of soils, friction angles range from 14° to 33°, and represent a broad range of well–sediment interactions.

2.3.3 Code verification

The fully coupled hydro-mechanical finite element code was verified against analytically tractable cases, including: self-weight consolidation under 1D conditions, radial flow (perfectly rigid porous medium of constant permeability), and sediment–casing interaction (as a loaded perfectly rigid pile foundation in an elasto-plastic medium—with and without tip resistance). In all cases, numerical predictions were in full agreement with available solutions.

2.3.4 Depressurization

Depressurization Δu is simulated by reducing the fluid next to the well along the production zone from the initial hydrostatic condition u_o to a value $u_o - \Delta u$. For equilibrium, the internal pressure imposed onto steel faces inside the casing is reduced by the same amount Δu beneath the isolation plate. Above the isolation place, the internal hydrostatic pressure imposed onto steel faces inside the casing remains at the initial values before production $u_o(z)$.

3 Parametric study: numerical results

3.1 Field case

The simulated field case represents conditions relevant to known hydrate accumulations in marine sediments that have been considered for production. The 156-m-long well is modeled as a constant diameter pipe ($d = 127$ mm, wall thickness 27 mm). The hypothetical production horizon rests between 140 and 155 mbsf (typically in Ulleung basin); thus, a 15-m-long production screen is modeled between $z = 140$ and $z = 155$ mbsf (Fig. 1). A

depressurization of $\Delta u = -6$ MPa is gradually imposed (24 h ramp up) and kept constant thereafter. The depth of water above the sediment column cancels out in the hydro-mechanical analysis conducted here; therefore, results apply to any water depth $z_w \geq \Delta u/\gamma_w$. The simulation domain extends to a radial distance of 600 m away from the well and to a depth of 300 mbsf.

The elongated geometry of the well, the need for fine-meshing next to the well and in zones of high stress gradients, and the required faraway boundaries combine to produce a simulation that requires 60,000 nodes and 20,000 elements (Fig. 1).

The four sediments considered for this study include a sandy sediment, low and high plasticity clays, and a diatomaceous sediment; these capture the breadth of hydrate-bearing sediments in marine formations (Gulf of Mexico, Krishna-Godavari basin, Ulleung Basin and Nankai Trough) and in the permafrost (Mt. Elebert—Alaska). Constitutive model parameters summarized in Table 1a form a self-consistent set of values based on our own laboratory characterizations of these sediments and extensive databases that include a large number of published studies [4, 25], and references therein.

3.2 General trends from numerical results

The set of numerical results presented in this manuscript are representative of the complete parametric study and readily illustrate salient observations. Figure 2 shows general trends for sandy sediment. Contour plots are restricted to the 50×50 m region around the well where most pronounced changes take place. It can be observed that

- Depressurization affects a relatively narrow region around the well (Fig. 2a); in fact, only 50 % of the depressurization Δu imposed at the well remains at a radial distance of about $r \approx 1$ m from the well (detailed plots later in this manuscript).
- Significant radial strains take place in a region limited to a radial distance similar to the thickness of the production horizon (Fig. 2b). Close to the well, a relatively narrow sediment annulus experiences horizontal contraction against the screen/pack driven by seepage forces, and forms a compact "shell." Further away, the sediment undergoes radial extension (needed to make the inner shell contraction compatible with static conditions in the far field).
- There is vertical extension near the well at the top and at the bottom of the production horizon (Fig. 2c); in fact, the sediment beneath the production horizon swells up (Fig. 2d).
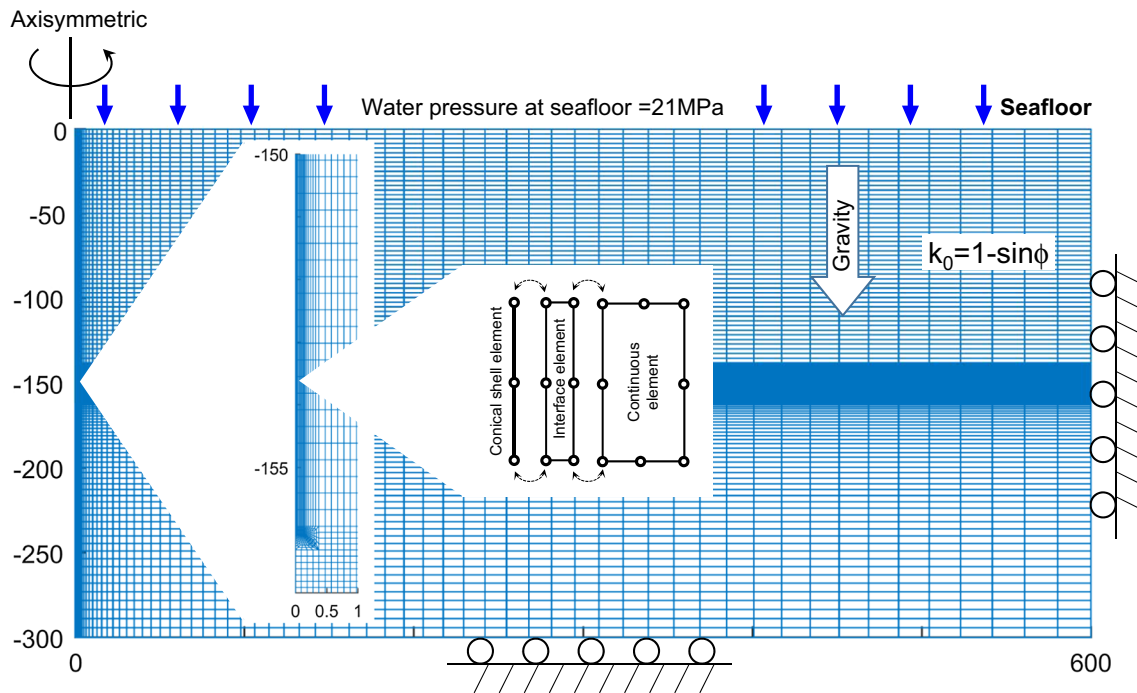
Fig. 1 Numerical model: boundary conditions, initial conditions and model geometry. Successive zoom-ins show the higher discretization within the production horizon and details at the sediment–well interface
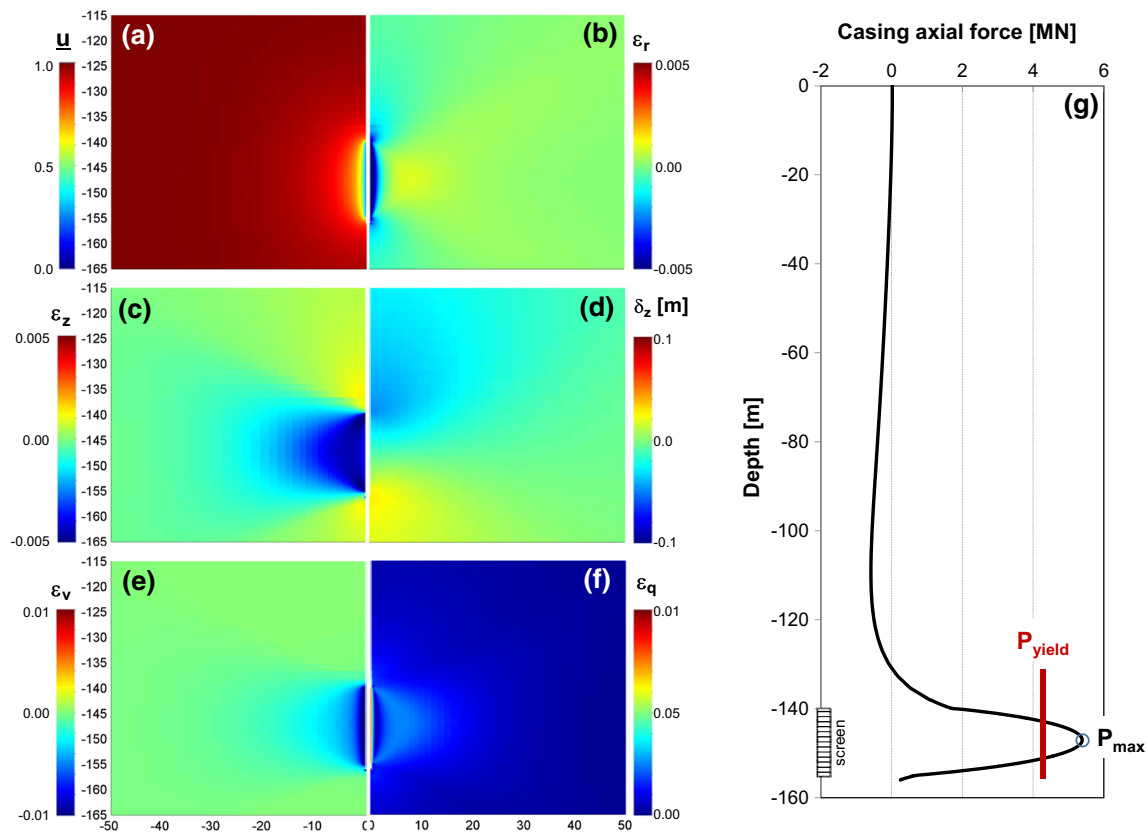

Fig. 2 Sediment–well interaction during depressurization (Case: sandy sediment—parameters in Table 1): **a** normalized pressure $\underline{u} = (u - u_{well})/(u_{far} - u_{well})$, **b** radial strain, **c** vertical strain, **d** vertical displacement, **e** volumetric strain (negative = compaction), **f** shear strain, **g** axial force distribution along the casing (negative = tension)

Table 1 Selected sediments: (a) constitutive parameters (b) Layer compaction for 1D conditions versus computed settlement

Modified Cam-Clay—associated flow rule		Plastic clayey sediment	Low IP clayey sediment	Diatomaceous sediment	Sandy sediment
a. Constitutive model					
Frictional strength	ϕ	14°	22°	27°	33°
Permeability (Eq. 2 in text))	e_{ref}	1.0	1.0	1.0	1.0
$\frac{k}{k_{ref}} = \left(\frac{e}{e_{ref}}\right)^b$	k_{ref}	10^{-10} cm/s	10^{-7} cm/s	10^{-9} cm/s	10^{-2} cm/s
	b	4.2	3.8	6	3.0
Compressibility (Eq. 1 in text)*	e_{1kPa}	4.8	1.7	4	0.8
$e = e_{1kPa} - C_c \log\left(\frac{1\,kPa}{\sigma' + \sigma'_L} + \frac{1\,kPa}{\sigma'_H}\right)^{-1}$	C_c	1.4	0.4	0.8	0.1
	e_L	4.0	1.4	3.6	0.7
	e_H	0.1	0.2	0.3	0.4
b. Layer compaction and settlement					
1D compaction					
Production layer compaction (m)		4.39	1.77	3.89	0.50
Wellbore production analysis					
Seabed settlement (cm)		5.6	7.2	7.8	0.6
Production layer compaction (cm)		13.0	16.6	18.6	7.0

Compaction of a 15-m-thick layer between 140 and 155 mbsf. A depressurization of $\Delta u = 6$ MPa is imposed everywhere in the layer

* $\sigma'_H = 10^{\frac{e_{1kPa} - e_H}{C_c}} \cdot$ kPa and $\sigma'_L = \sigma'_H / 10^{\frac{e_L - e_H}{C_c}} - 1$. Poisson's ratio $\upsilon = 0.3$. Recompression: $C_r = 0.2 C_c$

- Radial and vertical strains combine into volumetric and deviatoric strains (Fig. 2e, f). Volumetric contraction is high, yet the affected zone is limited to a narrow region around the well. Deviatoric strains are highest around the screen/pack and at the tip of the well. Stresses arch around the contracted zone (not shown). Due to the local effect of depressurization, the vertical settlement above the production horizon is significantly smaller than the 1D settlement computed for the affected layer subjected to the same depressurization.

- The sediment shears along the interface with the casing, and it transfers load onto the casing during vertical contraction (Fig. 2g). The peak axial load P_{max} in the casing takes place within the production horizon, and it may exceed the yield capacity of the casing P_{yield}. Arching around the depressurized zone means that the casing "hangs" from the upper part of the sediment and develops tension.

3.3 Importance of compressibility-conductivity in hydro-mechanical coupling

The coupled hydro-mechanical FEM model exposes the complex nature of sediment–well interaction during depressurization. In particular, the rapid pressure recovery away from the well is due in part to geometric effects (Laplacian), yet it is exacerbated by changes in permeability associated with compaction (Eqs. 1, 2). Strong hydro-mechanical coupling between fluid pressure, effective stress, void ratio and permeability $u - \sigma' - e - k$ should be expected for clayey sediments as they are more compressible (higher C_c coefficient in Eq. 1) and their permeability is more susceptible to changes in void ratio (higher b-exponent in Eq. 2).

Results in Fig. 3 show that a higher b-exponent (at the same compressibility C_c) results in a narrower depressurization field, lower settlements and lower axial forces in the casing. In particular, the assumption of a constant hydraulic conductivity k (i.e., $b = 0$) could lead to a gross overestimation of the axial force in the casing.

The formation of a compact sediment shell around the screen/pack in more compressible sediments (higher C_c and b-exponent) can have a prevalent effect on the system response and may lead to a counterintuitive response as shown in Fig. 4: Compared to the low plasticity clay, the more compressible "high plasticity" clay develops a tighter sediment shell around the screen/pack, pressure recovers closer to the well, the vertical settlement is smaller in the more compressible sediment, and a lower axial load builds on the casing (parameters in Table 1a—Note: Differences in friction angle can justify a ratio in peak loads of ~0.7 between the two cases).

3.4 Strata-bound layered reservoir

Hydrate accumulations preferentially take place in the more pervious sandy layers bound within fine-grained sediments [5]. Furthermore hydrate reservoirs are often found in diatomaceous sediments, such as in the Ulleun Basin [35]. These unique formations have exceptionally high void ratio, and their hydraulic conductivity is very
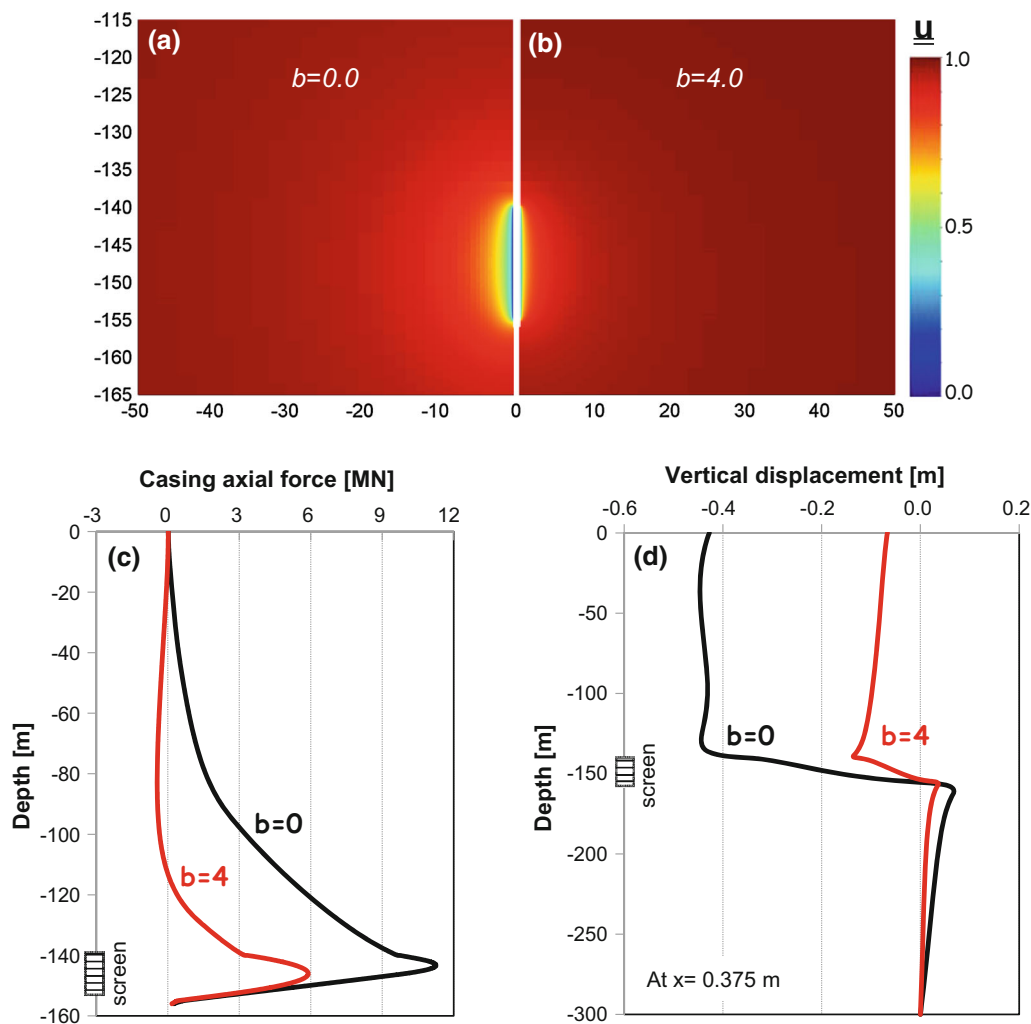
Fig. 3 Hydro-mechanical coupling—stress-dependent permeability. Case: low plasticity clayey sediment with either constant permeability $b = 0$ or void ratio-dependent permeability $b = 4$ (All other parameters in Table 1). (**a**, **b**) normalized fluid pressure $\underline{u} = (u - u_{well})/(u_{far} - u_{well})$, **c** axial force distribution along the casing (negative = tension), and **d** vertical displacement measured at a radial distance $x = 0.375$ m

sensitive to changes in void ratio during compaction, i.e., high b-exponent in Eq. 2 [14].

Figure 5 compares the pressure field at steady state during depressurization in a homogeneous diatomaceous sediment and when a 5-m-thick sandy layer is buried within the diatomaceous sediment. The low-compressibility sandy layer does not form a tight shell around the well, but the diatomaceous sediment above and below compact against the sand layer to form a low-permeability skin that reduces leak-in from the diatomaceous sediment into the production horizon. Consequently, (1) depressurization extends further away into the sandy layer and affects a relatively large region away from the well; (2) the presence of a sandy layer leads to higher overall settlement (Fig. 5c); and (3) a higher axial force develops on the casing (in part due to higher friction angle).

3.5 Axial force in the casing

The casing sustains tension in the upper part (negative values) and maximum compression within the production horizon (positive—Figs. 2, 3 and 4). The compression bulb that forms around the well during depressurization enlarges during early stages of production (i.e., during pressure diffusion and before steady-state seepage), and the peak tensile force in the casing reaches a maximum value and then gradually decreases and moves upwards until steady-state conditions are reached. In all cases run for this study, the maximum transient tensile force was not sufficient to cause the tensile failure of the continuous casing, but could cause significant localized slippage and displacement in joints/connectors above the production zone.
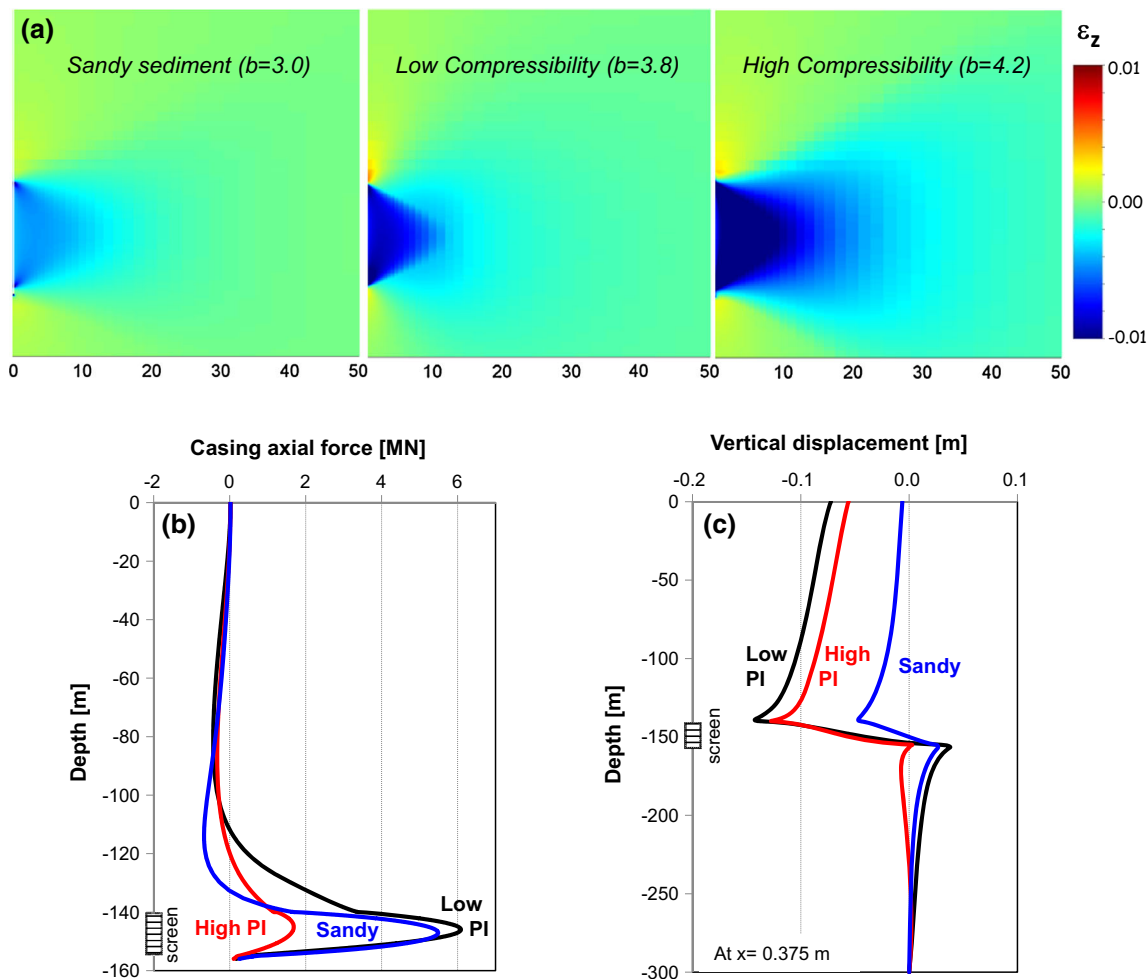
Fig. 4 Effect of sediment compressibility and void ratio-dependent permeability. Cases: sandy sediment, low and high plasticity clayey sediments (All parameters in Table 1): **a** vertical strain, **b** axial force distribution along the casing (negative = tension), **c** vertical displacement measured at a radial distance $x = 0.375$ m

3.6 Settlement

The settlement experienced by the production horizon and the settlement that reaches the seafloor are surprisingly similar in the four sediments studied here (Table 1b). This result highlights the tradeoff between high compressibility (high strains) and high void ratio-dependent permeability (smaller affected volume). For comparison, Table 1 includes the 1D settlement that the 15-m-thick layer between 140 and 155 mbsf would experience if subjected to a homogeneous depressurization of $\Delta u = 6$ MPa: computed 1D settlements do scale with compressibility C_c (as per Eq. 1) and are more than an order of magnitude larger than the actual settlement computed using a formal analysis of hydro-mechanical coupling in well–sediment interaction.

Hydrate-bearing sediments in permafrost are subjected to higher initial effective stresses than marine sediments and should experience lesser hydro-mechanical coupling

effects. Still, high axial forces will buildup in the casing and careful analysis and proper engineering are required.

4 Simplified analysis: bounds

Simpler yet robust solutions are often used in casing engineering. Three levels of simplification are explored next including elastic and rigid sediment models, and bound estimates of axial force in the casing.

4.1 Linear–elastic sediment in FEM

Let's replace the Modified Cam-Clay model in the FEM simulator for a simpler linear–elastic medium. In order to maximize the potential similarity between the two models: (a) The stiffness varies with depth E_z in the elastic model, (b) the elastic stiffness at each depth after self-weight consolidation is computed as the tangent of the
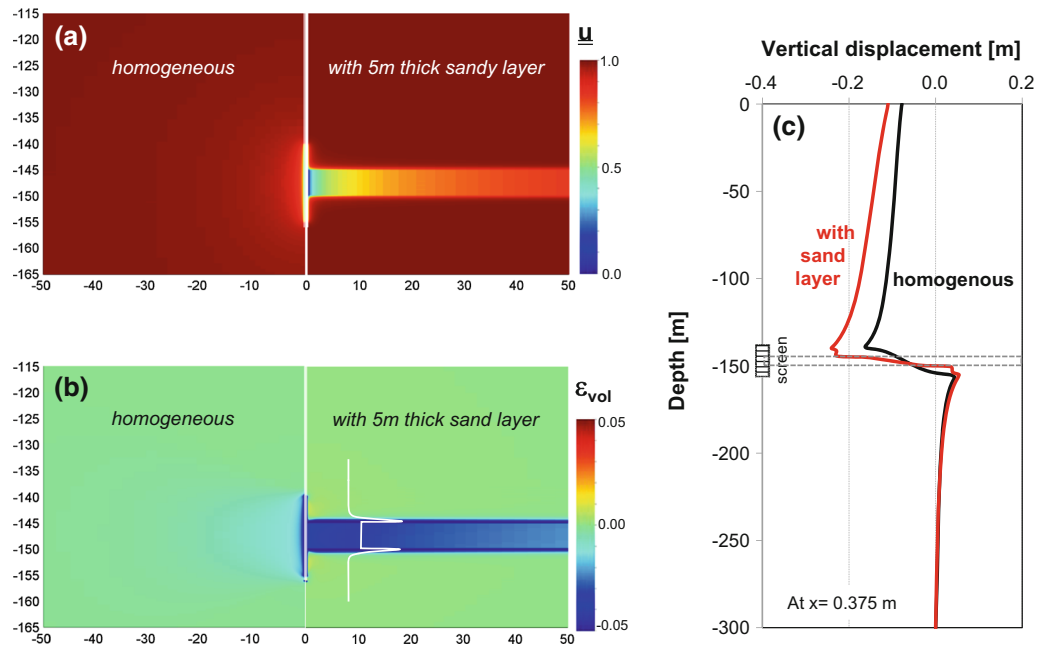
Fig. 5 Homogeneous versus layered formation. Case: diatomaceous formation with and without a 5-m-thick sand layer (All parameters in Table 1): **a** pore fluid pressure, **b** volumetric strain, **c** vertical displacement measured at a radial distance $x = 0.375$ m
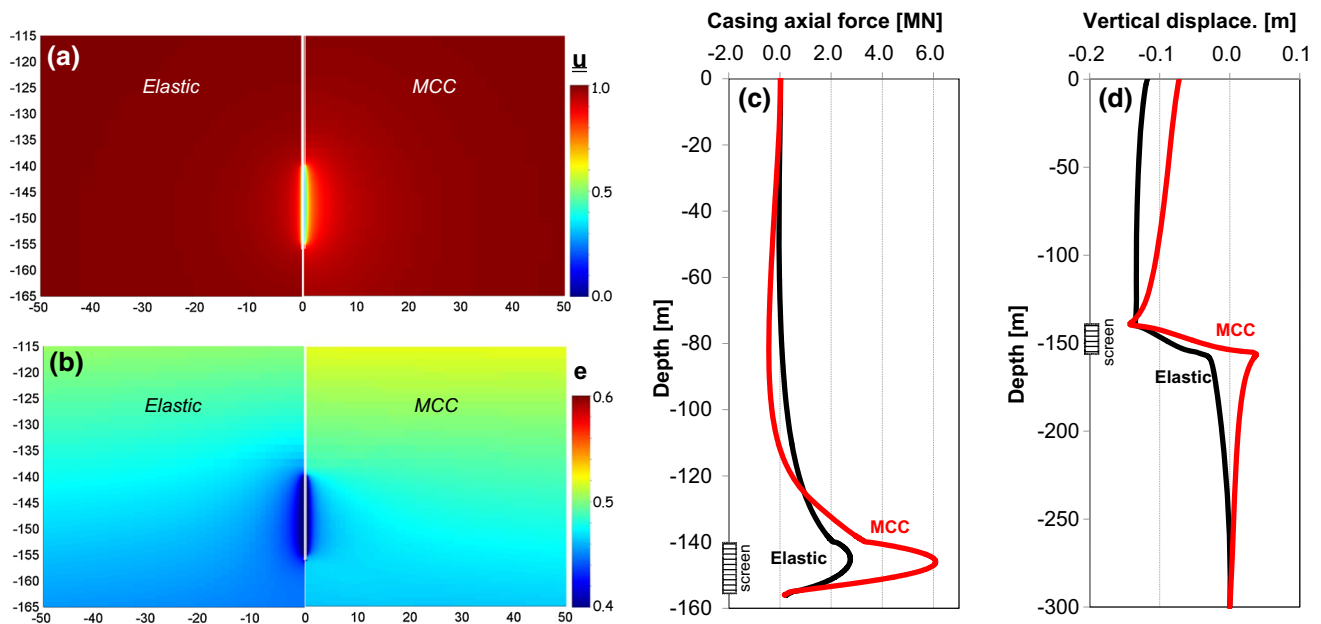

Fig. 6 Sediment representation: elastic model versus Cam-Clay model. Initial parameters before depressurization are identical in both cases, including the tangential stiffness. Case: low plasticity clayey sediment (parameters shared by both models are listed in Table 1): **a** normalized pressure, $\underline{u} = (u - u_{\text{well}})/(u_{\text{far}} - u_{\text{well}})$, **b** void ratio e, **c** axial force distribution along the casing (negative = tension), and **d** vertical displacement measured at a radial distance $x = 0.375$ m

compressibility $E_z = 3(1 - 2\nu)[(1 + e_z)/\lambda)]\sigma'_z$ and (c) the stiffness E_z remains constant during depressurization. Consequently, the initial asymptotic conditions are identical for both linear–elastic and Modified Cam-Clay models at the beginning of depressurization. Furthermore, the simplified simulations employ the same void ratio-dependent permeability (Eq. 2) and the same elasto-plastic

sediment–casing interface (Eq. 3) as the numerical solutions with Cam-Clay. While numerical results show similar trends (see Fig. 6), the casing experiences higher peak tensile and compressive axial forces when the nonlinear Cam-Clay model is used. Similar results were obtained with all cases run as part of the parametric study conducted for this investigation.

4.2 Rigid soil model

Equilibrium conditions relate the change in the casing axial force P_z [N] at depth z [m] to the mobilized shear resistance against the casing τ_z [kPa] at the same depth,

$$\frac{\partial P_z}{\partial z} \mathrm{d}z = -\pi \, d_{well} \, \tau_z \, \mathrm{d}z \tag{5}$$

This equation can be readily solved in finite differences

$$P_i - P_{i+1} = -(\pi d_{well} \, \Delta z) \, \tau_i \tag{6}$$

This approach is frequently used in pile–soil interaction analyses. Its implementation to the analysis of sediment–well interaction assumes that the sediment column above the production layer is a perfectly rigid body that settles a prescribed amount across the production horizon. Flow and flow-induced layer compression are not simulated in this case; instead an estimate of the layer compaction is selected as input parameter. The solution is sensitive to values selected for yield displacement δ_y (must be different to the value used in 3D FEM to account for sediment deformation), settlement of the production horizon (as discussed above, it cannot be the 1D settlement of the layer due to localized depressurization), and tip stiffness and bearing capacity. Therefore, gains in model simplicity come with the need for more insightful selection of model parameters; otherwise, results that appear to be mechanically correct can be critically erroneous.

4.3 Bounds for the axial force in the casing

Numerical results show that settlement within and around the production horizon causes the sediment above the produced layer to drag the well down, building longitudinal axial load in the casing. In long wells, the maximum load a well can develop P_{max} is limited by the upward shear resistance τ_z that can be mobilized in the production layer plus the tip resistance P_{tip} generated against the resting layer, and the yield capacity of the casing P_{yield}

$$\begin{aligned} P_{max} &\leq P_{tip} + 2\pi R \int\limits_{layer} \tau_z \, \mathrm{d}z \\ &\leq P_{yield} = A_m \sigma_y \end{aligned} \tag{7}$$

where A_m is the material cross section of the casing and σ_y is the yield stress of steel. The value of P_{max} is mobilized at the top of the production horizon.

5 Discussion–implications

5.1 Reduced production zone

Hydro-mechanical coupling and the development of a compact shell around the well combines with radial flow conditions to cause a fast recovery of the pressure field near the well. Figure 7 shows the steady-state pressure field radially away from the well at mid-height of the producing layer. Pressure trends are shown for two values of the b-exponent in the hydraulic conductivity vs. void ratio Eq. 2. It can be observed that higher depressurization at the well Δu results in a more compact shell around the screen/pack (Fig. 7a): The normalized pressure field recovers at a shorter radial distance when $\Delta u = 6$ MPa than when $\Delta u = 1$ MPa. Also, finer sediments with higher hydro-mechanical coupling (higher b-exponent) exhibit a more rapid decrease in pressure (Fig. 7a, b)
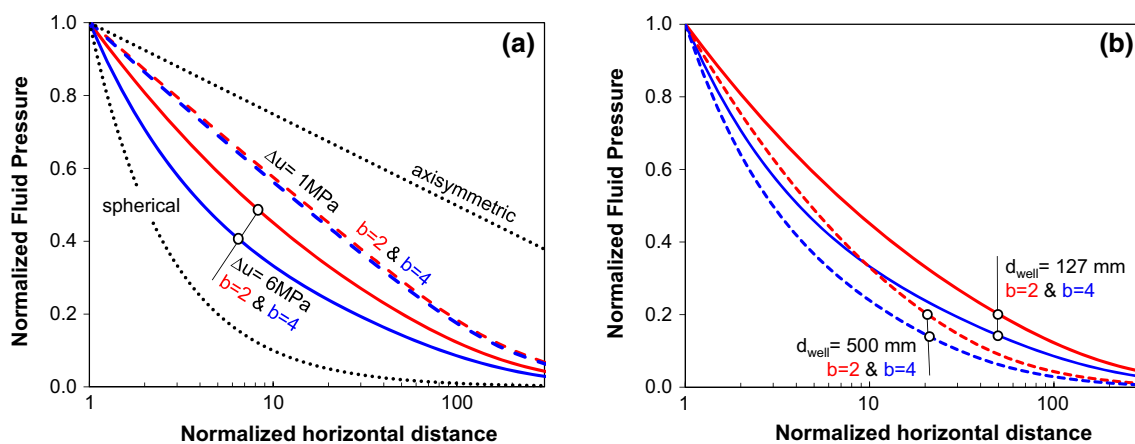

Fig. 7 Fluid pressure distribution away from the well at the center of the production horizon. Case: low plasticity clayey sediment of low and high b-exponent (Other parameters in Table 1). Normalized fluid pressure $\underline{u} = (u - u_{well})/(u_{far} - u_{well})$. **a** Small well diameter ($d_{well} = 127$ mm) subjected to a depressurization of $\Delta u = 1$ MPa and $\Delta u = 6$ MPa. **b** Enlarged "effective well diameter"

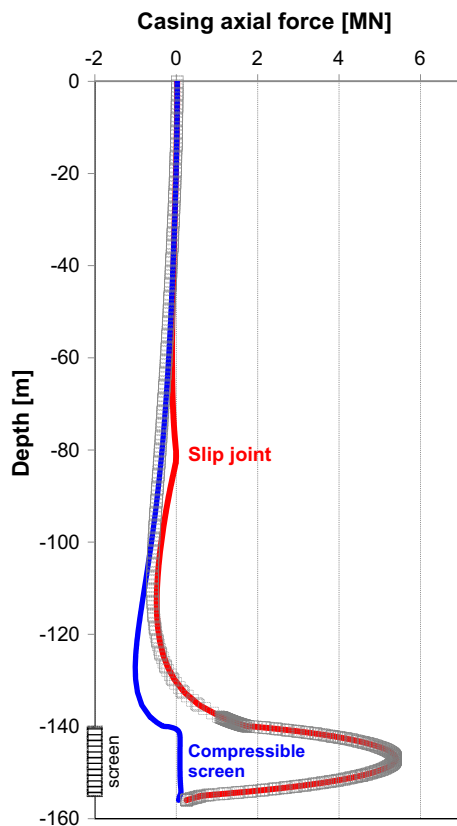## Casing axial force [MN]

Fig. 8 Well engineering to reduce axial load (Case: sandy sediment—all parameters in Table 1). The continuous well (square data points) is modified to reduce the buildup of tension by including a slip joint above the production horizon at $z = 80$ m (*red*), or to reduce the buildup of high compressive forces using a "soft" screen design within the production horizon (*blue*)

5.2 Enlarged gravel pack

Additional simulations were run with a 4 times larger well diameter in the production horizon to account for an enlarged gravel pack around the well. Pressure trends gradually converge away from the well: The size of the zone affected by 50 % of the depressurization imposed at the well is only 2.5 times larger in the case of the enlarged well, even though the well diameter is 4 times larger. Gas production increases with either the square (radial axisymmetric) or the cube (spherical) of the affected radius and may justify efforts to attain an enlarged effective well size around the screen.

5.3 Casing design features

Numerical simulations with strategically located soft casing elements were run to simulate slip joints above the production horizon to reduce tension and compressible telescopic-sliding screens to minimize the buildup of compressive axial force in the casing (Note: The reduction

of sediment-casing friction has physical limitations and limited impact). Results presented in Fig. 8 confirm the efficiency of "soft" features along the casing and help identify the displacement they need to accommodate; for example, the single slip joint at depth $z = 80$ m should allow for 1.2 cm displacement.

Finally, we note that horizontal wells within the production horizon can minimize the generation of compressive axial forces in the casing and significantly enlarge the volume subjected to depressurization; however, hydromechanical coupling effects should be properly taken into consideration in such production systems as well.

6 Conclusions

This study explored the implications of depressurization on sediment–well interaction. While the methodology is of general validity, the simulated cases reflect conditions that would be encountered in the context of gas production from hydrate-bearing marine sediments where the initial effective stress σ'_o is low and depressurization Δu is high so that $\Delta\sigma' > \sigma'_o$. Results show:

- Hydro-mechanically coupled analysis must capture the circular link between depressurization $\Delta u \rightarrow$ increased effective stress $\sigma'u \rightarrow$ sediment compaction $\rightarrow$ reduced hydraulic conductivity due to compaction $\rightarrow$ altered pressure field $u(r, z)$, and so on.
- Hydro-mechanical coupling plays a critical role in sediment-well response when soft sediments are subjected to high depressurization. Adequate constitutive models are needed to capture sediment compaction and the evolution of hydraulic conductivity during depressurization.
- A compacted low-permeability shell forms against the screen/pack. This shell reduces the size of the region affected by depressurization, the potential for gas production, and overall settlement. In fact, the higher the sensitivity of hydraulic conductivity to compaction, the narrower the production zone becomes.
- High compressive axial forces arise in the casing; the maximum compressive force develops within the production horizon. Compression may cause the casing to yield and even collapse. The assumption of a constant hydraulic conductivity k leads to a gross overestimation of the axial force in the casing.
- A tensile force develops in the casing above the production horizon as the compacted sediment in the depressurized volume pulls down from the well. The maximum tensile force occurs before steady-state conditions are reached.

- The application of simplified sediment-well analyses such as elastic or rigid sediment models requires insightful understanding of the underlying hydro-mechanical coupled processes for the selection of adequate simulation parameters. Therefore, simplified approaches must be avoided for the analysis of sediment–well interaction when a high depressurization/stress ratio $\Delta u/\sigma'_o$ is imposed.

- The engineering design of wells used for depressurization in soft sediments should: (1) accommodate extensional displacement in the well above the production horizon, e.g., with slip joints; (2) create soft screen conditions to avoid the buildup of compressive axial force in the casing within the production horizon, e.g., telescopic, sliding or folding design, and (3) incorporate an enlarged gravel pack around the screen to extend the production zone. Horizontal wells minimize the generation of compressive axial forces; however, they remain affected by other hydro-mechanical coupled effects.

References

1. Anderson BJ, Kurihara M, White MD, Moridis GJ, Wilson SJ, Pooladi-Darvish M, Gaddipati M, Masuda Y, Collett TS, Hunter RB, Narita H, Rose K, Boswell R (2010) Regional long-term production modeling from a single well test, Mount Elbert gas hydrate stratigraphic test well, Alaska North slope. Mar Pet Geol 28(2):493–501

2. Carrier WD (2003) Goodbye Hazen; Hello Kozeny-Carman. J Geotech Geoenviron Eng ASCE 129(GT 11):1054–1056

3. Chapuis RP (2012) Predicting the saturated hydraulic conductivity of soils: a review. B Eng Geol Environ 71(3):401–434

4. Chong SH, Santamarina JC (2016) Soil Compressibility Models for Wide Stress Range. J Geotech Geoenviron Eng ASCE (Published on line 3/2016)

5. Cook AE, Malinverno A (2013) Short migration of methane into a gas hydrate-bearing sand layer at Walker Ridge. Geochem Geophys Geosyst 14:283–291. doi:10.1002/ggge.20040

6. Dolinar B (2009) Predicting the hydraulic conductivity of saturated clays using plasticity-value correlation. Appl Clay Sci 45:90–94

7. Feia S, Sulem J, Canou J, Ghabezloo S, Clain X (2016) Changes in permeability of sand during triaxial loading: effect of fine particles production. Acta Geotech 11:1–19

8. Gamwo IK, Liu Y (2010) Mathematical modeling and numerical simulation of methane production in a hydrate reservoir. Ind Eng Chem Res 49:5231–5245

9. Gens A, Potts DM (1988) Critical state models in computational geomechanics. Eng Comput 8(3):178–197

10. Hong H, Pooladi-Darvish M (2003) A numerical study on gas production from formations containing gas hydrates. In: Canadian international petroleum conference-54th Annual technical meeting, June 10–12, Calgary, Canada

11. Klar A, Uchida S, Soga K, Yamamoto K (2013) Explicitly coupled thermal flow mechanical formulation for gas-hydrate sediments. SPE J 18(02):196–206

12. Kurihara M, Sato A, Ouchi H, Narita H, Masuda Y, Saeki T, Fujii T (2009) Prediction of gas productivity from eastern Nankai Trough methane hydrate reservoirs. SPE J Reserv Eval Eng 12:477–499

13. Kwon TH, Cho GC, Santamarina JC (2007) Hydrate dissociation in sediments: pressure-temperature evolution. Geochem Geophys Geosyst 9(2):Q03019. doi:10.1029/2007GC001920

14. Lee C, Yun TS, Lee JS, Bahk JJ, Santamarina JC (2011) Geotechnical characterization of marine sediments in The Ulleung Basin, East Sea. Eng Geol 117:151–158

15. Mesri G, Olson RE (1971) Mechanisms controlling the permeability of clays. Clay Clay Miner 19:151–158

16. Moridis GJ, Collett TS, Boswell R, Kurihara M, Reagan MT, Koh C, Sloan ED (2009) Toward production from gas hydrates: assessment of resources, technology, and potential. SPE Journal 12(5):745–771. doi:10.2118/114163

17. Moridis GJ, Collett TS, Pooladi-Darvish M, Pooladi-Darvish M, Santamarina C, Boswell R, Kneafsey TJ, Rutqvist J, Reagan MT, Sloan ED, Sum A, Koh C (2011) Challenges, uncertainties, and issues facing gas production from gas-hydrate deposits. SPE Res Eval Eng 14(1):76–112. doi:10.2118/131792-PA

18. Moridis GJ, Sloan ED (2007) Gas production potential of disperse low-saturation hydrate accumulations in oceanic sediments. Energy Convers Manag 48:1834–1849

19. Moridis GJ, Kowalsky MB, Pruess K (2007) Depressurization-induced gas production from class 1 hydrate deposits. SPE J Reser Eval Eng 10:458–481

20. Moridis GJ, Silpngarmlert S, Reagan MT, Collett T, Zhang K (2010) Gas production from a cold, stratigraphically-bounded gas hydrate deposit. Mar Pet Geol. doi:10.1016/j.marpetgeo.2010.01.005

21. Muir Wood D (1990) Soil behaviour and critical state soil mechanics. Cambridge University Press, Cambridge

22. Nazridoust K, Ahmadi G (2007) Computational modeling of methane hydrate dissociation in a sandstone core. Chem Eng Sci 62:6155–6177

23. Poulos HG, Davis EH (1980) Pile foundation analysis and design. Wiley, Hoboken

24. Raju IS, Rao BP, Venkataramana J (1974) A conical shell finite element. Comput Struct 4:901–915

25. Ren X-W, Santamarina JC (2006) The hydraulic conductivity in sediments. ASCE Geotech J (Under review)

26. Samarasinghe AM, Huang YH, Drnevich VP (1982) Permeability and consolidation of normally consolidated soils. J Geotech Eng Div 108(GT6):835–850

27. Sánchez M, Shastri A, Santamarina JC, Gai X (2014) Coupled modeling of gas hydrate bearing sediments. In: 14th International conference of the international association for computer methods and advances in geomechanics, 14th IACMAG. Kyoto

28. Schofield AN (1980) Cambridge University geotechnical centrifuge operations. Getech 30(3):227–268

29. Segura JM, Carol I (2004) On zero-thickness interface elements for diffusion problems. Int J Numer Anal Meth Geomech 28(9):947–962

30. Simo JC, Taylor RL (1985) Consistent tangent operators for rate-independent elastoplasticity. Comput Methods Appl Mech Eng 48:101–118

31. Sloan ED, Koh CA (2008) Clathrate hydrates of natural gases, 3rd edn. CRC Press, Boca Raton

32. Uddin M, Coombe D, Law D, Gunter B (2008) Numerical studies of gas hydrate formation and decomposition in a geological reservoir. J Energy Res Technol 130:032501

33. Wilder JW, Moridis GJ, Wilson SJ, Kurihara M, White MD, Masuda Y, Anderson BJ., Collett TS, Hunter RB, Narita H, Pooladi-Darvish M, Rose K, Boswell R (2008) An international effort to compare gas hydrate reservoir simulators. In: Proceedings of the 6th international conference on gas hydrate, July 6–10 Vancouver, Canada

34. Yu HS (2006) Plasticity and geotechnics. Springer, New York

35. Yun TS, Lee C, Lee JS, Bahk JJ, Santamarina JC (2011) A pressure core based characterization of hydrate bearing sediments in the Ulleung Basin East Sea. J. Geophys. Res. 117:151–158. doi:10.1029/2010JB007468